Reservoir Rock Typing for Heterogeneous Sandstone: A Case Study of Nubia Sandstone, Gulf of Suez, Egypt

Mohamed S. El Sharawy *

Posted Date: 15 April 2026

doi: 10.20944/preprints202604.1026.v1

Keywords: reservoir rock type; Nubia sandstone; Gulf of Suez; lithofacies; machine learning

 doi:10.20944/preprints202604.1026.v1

Article

Reservoir Rock Typing for Heterogeneous Sandstone: A Case Study of Nubia Sandstone, Gulf of Suez, Egypt

Mohamed S. El Sharawy

National Research Centre, Cairo, Egypt; sharawy2001@hotmail.com

Abstract

The pre-Cenomanian Nubia sandstone is considered as one of the most productive reservoirs in the Gulf of Suez, Egypt. Determination of its reservoir rock type (RRT) is a crucial process in reservoir characterization and modeling, especially when the reservoir is extremely heterogeneous. In this study, an effort was made to bridge the gap between various techniques to determining RRT, which include lithofacies, traditional methods (x-y crossplots), and machine learning (ML). To accomplish this, the objectives of this study were accomplished through the utilization of sedimentological core description, routine core analysis, and conventional logging data from two wells (well A and well B) in the southern Gulf of Suez. The results show that the complete Nubia interval in the southern Gulf of Suez can be distinguished into seven distinct lithofacies (LF1-LF7). The first six lithofacies are comprised of different types of sandstones, while the seventh is related to mudstone. The results show also that the fault-cutting, rather than stratigraphic reasons, was primarily responsible for the difference in Nubia thicknesses between the two studied wells. It is likely that the lower three lithofacies were separated from one another by unconformity surfaces. The traditional techniques used to predict the RRTs show that the normalized reservoir quality index (NRQI) was the most appreciated method to predict the Nubia rock types. On the other hand, K –means clustering and self-organizing maps (SOM) techniques based on raw logging data and principal component analysis (PCA) can properly predict the Nubia reservoir rock types when correlated with the Ward's method, which is based on the core data. The reservoir rock quality ranged from poor to very good, with a domination of moderate reservoir quality in well A and very good reservoir quality in well B. This discernible difference in reservoir quality between the two wells was probably attributed to the consequences of the post-deposition diagenesis processes and the variation of the sandstone texture.

Keywords: reservoir rock type; Nubia sandstone; Gulf of Suez; lithofacies; machine learning

1. Introduction

Reservoir rock typing is crucial for the reservoir characterization process. For carbonates and heterogeneous clastic rocks, rock typing is essential for reservoir simulation and management. Core analysis is the basis for the direct determination of rock type, whereas well logs are used for the indirect one. Although there is no consistent definition for rock type, Gunter et al. [1] introduced the most acceptable rock type definition. According them, rock type is defined as "units of rock deposited under similar conditions that experienced similar diagenetic processes resulting in a unique porosity (ϕ)-permeability (k) relationship, capillary pressure profile, and water saturation for a given height above free water in a reservoir". This definition could be a modified form of the rock type definition described by [2], in which he defined the rock type as "a formation whose parts have been deposited under similar conditions and have undergone similar processes of later diagenesis". After discussing the relationships between rock types and other petrophysical properties, he stated that several rock types may have the same pore size distribution.

 doi:10.20944/preprints202604.1026.v1

Determining rock types involves several methods. These methods may be predicated on geological attributes (depositional facies and diagenesis), petrophysical attributes (porosity, permeability, grain size, and capillary pressure curves), or production large-scale dynamic data [3]. Rushing et al. [4] introduced the terms "depositional rock types" to represent the large-scale geologic framework and the original rock properties present at deposition; "petrographic rock types" which are similar to the depositional one but are based on the pore-scale microscopic imaging; and "the hydraulic rock types" which are based also on the pore-scale but represent the physical properties of the rock, such as porosity, permeability, and capillary pressure.

Based on capillary pressure curves, Leverett [5] and Thomeer [6] differentiated the reservoir into rock types. The former introduced the J-function to universalize the capillary pressure curves, including the mean hydraulic radius in the equation. On the other hand, Thomeer [6] introduced the pore geometrical factor to define the shape of the capillary pressure curve and indirectly the rock type. Other benefits of capillary pressure curves were discovered by [7–9]. They each investigated the relationship between permeability, porosity and pore throat radius. They formulated their studies into empirical equations known as R_{35} (the effective pore system that dominates flow through a rock corresponds to a mercury saturation of 35%) for the first two authors and R_{20} for the third author. Buckles [10] considered that initial water saturation (S_{wi}) times porosity (ϕ) yielded constant (C) that corresponded to a distinct rock type. The curve can be potted using an arithmetic scale or a logarithmic scale.

Asquith and Gibson [11] used well log crossplots such as neutron porosity vs. true formation resistivity and sonic porosity vs. true formation resistivity. The clusters that were generated indicated certain rock types that had been previously identified through core or cuttings analysis. The breakthrough was carried out by [12]. Based on the Kozeny-Carman equation, they introduced a theoretical relationship that related porosity to permeability. Using core porosity and permeability, they introduced the terms reservoir quality index (RQI), flow zone indicator (FZI), and hydraulic flow unit (HFU). Each average value of FZI defines a HFU. Additionally, they introduced an equation that uses the average value of FZI to predict permeability in uncored intervals. Discrete rock type (DRT) is usually used to round FZI values. The approach of Amaefule et al. [12] was modified by several authors, such as [13–17]. Based on the value of FZI, Corbett and Potter [18] introduced a type curve known as a global hydraulic element (GHE). They plotted porosity against permeability in a semi-log plot producing ten GHEs; each GHE is distinguished by its respective color. Wibowo and Permadi [19] introduced an additional type curve plot to determine the rock types. This plot is a log-log plot of the pore geometry ($k/\phi^{0.5}$) against the pore structure (k/ϕ^3).

Rezaee et al. [20] introduced the term electrical flow units to define the zones with similar electrical properties. In their approach, they used the terms current zone indicator ($\mathrm{CZI} = \sqrt{\frac{\emptyset/_{\mathrm{F}}}{\emptyset_{\mathrm{Z}}}}$) and the electric radius indicator ($\mathrm{ERI} = \frac{\sqrt{\emptyset}}{\mathrm{F}}$). Where F is the formation resistivity factor and Φ_z is the normalized porosity ($\phi_z = (\frac{\emptyset}{1-\emptyset}$). For this method to be effective, F should be measured over a significant interval of the formation. Modification for this approach was carried out by several authors. Soleymanzadeh et al. [21] introduced a new parameter called the electrical quality index ($\mathrm{EQI} = \sqrt{\frac{1}{\mathrm{F}\emptyset}}$). Another modification was introduced by [22], in which they introduced the term electrical zone indicator ($\mathrm{EZI} = \frac{\mathrm{EQI}}{\emptyset_{\mathrm{Z}}}$). They used these parameters to identify the electrical rock types. Meanwhile, Mohammadi et al. [23] combined FZI and EZI into a single equation to identify reservoir rock types. Omrani et al. [24] introduced a new parameter called the characterization number ($\mathrm{Cn} = \sqrt{\frac{\ln k}{\emptyset}} * \mathrm{S_{wir}}$). They stated that each rock type has a constant Cn value.

 doi:10.20944/preprints202604.1026.v1

Recently, machine learning (ML) has become a key player in the rock typing process. ML can be either supervised or unsupervised. The main difference between the two types is that unsupervised machine learning algorithms uses unlabeled datasets while supervised learning uses labeled datasets. The supervised learning types could be classification or regression. On the other hand, the unsupervised learning algorithm categories can be grouped into the following: clustering (e.g., Hierarchical clustering and K-means), dimensionality reduction (e.g., principal component analysis), association rule learning (e.g., apriori algorithm), outlier detection (e.g., k-nearest neighbors), and density estimation (e.g., Kernel density estimation). Man et al. [25] used an unsupervised learning algorithm to identify HFUs and a supervised learning to predict HFUs using core and well log data. Mohammadian et al. [26] used both supervised and unsupervised learning to detect the optimum number of petrophysical rock types as well as to predict k and R_{35}. Mohammadinia et al. [27] used supervised learning, such as support vector machine (SVM), artificial neural network (ANN), and random forest (RF) to determine the HFUs and compare the results of each method with each other. Astsauri et al. [28] used unsupervised learning (K-means) and several supervised learning methods to predict FZI and consequently identify the reservoir HFUs. They concluded that using of ML in reservoir characterization is valuable, cost-effective, and offers precise results. Amosu et al. [29] employed unsupervised learning to predict electrofacies, thereby enabling them to differentiate between electrofacies that can produce hydrocarbons better than others. This paper aims to identify the RRTs of the heterogeneous Nubia sandstone reservoir using the sedimentological core description, traditional methods, and machine learning methods. The study also aims to ascertain the most dependable approach for identifying RRTs. One of the objectives of this study is to clarify the rock quality for each reservoir rock type. Additionally, the study intends to compare the impact on the resulting predicted RRTs of using raw well logging data, standardizing it using the principal component analysis (PCA) method, and normalizing it using the cumulative distribution function (CDF).

2. Geologic Setting

The Gulf of Suez (GOS), as a mature basin, is considered the most prolific hydrocarbon basin in Egypt. It can be seen as the northern extension of the Red Sea (Figure 1). The Oligocene-Early Miocene rift basin provides a valuable opportunity to investigate the interaction between several geologic (depositional environment, accommodation, diagenesis), tectonic (subsidence, uplift), and eustatic aspects of the evolution of the Gulf of Suez. The stratigraphic column extended from the Cambrian age till the Recent (Figure 2). The deposition of the Nubia sandstone unconformably on the basement rock was the result of the transgression phase that was predominant during the Paleozoic. Its age extended from the Cambrian to Lower Cretaceous. The Nubia sandstone is regarded as one of the most pay zones in the GOS. The Nubia sandstone was deposited in various environments, including shallow marine, fluvial braided and aeolian conditions. The degree of heterogeneity in the Nubia interval is primarily determined by variations in depositional conditions, sediment sources, and the impacts of post-depositional processes (compaction and diagenesis). According to El Sharawy [30], the Nubia interval ranged from strong to extremely heterogeneous. The heterogeneity can be traced vertically and laterally. Generally, the thickness of the Nubia sandstone is decreased southward. Shale streaks can be followed through the Nubia interval. The diagenesis of the Nubia sandstone played a major role in determining the quality of the reservoir. Several scholars, including [31,32], recognized six diagenetic processes, mostly led to reduction in both porosity and permeability. These diagenetic processes are compaction, pressure solution, cementation by silica, iron oxides, or carbonates, recrystallization, development of authigenic clay minerals, and replacement.

A transgression cycle from the Upper Cretaceous to Oligocene resulted in the main source rocks as well as some secondary reservoirs in the GOS. The Miocene interval recorded the main rift stage, in which reservoirs, source rocks, and seal rocks can be identified. Thick deposits can be encountered in the depocenters reached several kilometers, ranging from clastics, carbonates, and evaporites.

 doi:10.20944/preprints202604.1026.v1

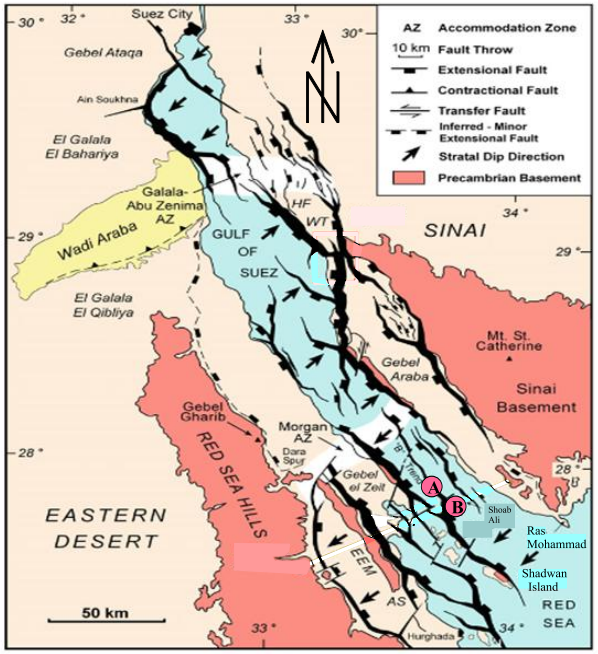

Figure 1. Tectonic map of the Gulf of Suez showing the main structural elements as well as the location of the two studied well (well A and well B) (modified after [33]).

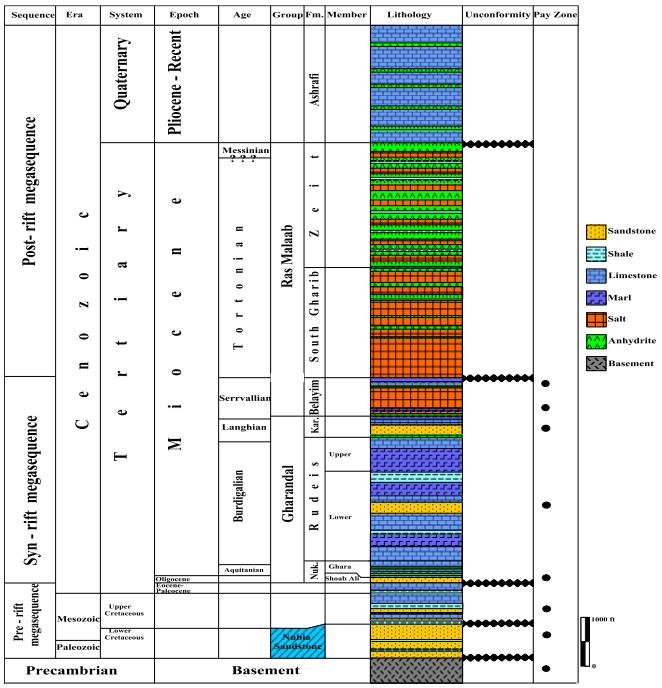

Figure 2. The generalized stratigraphic column of the southern Gulf of Suez.

The GOS tectonic evolution was passed through several stages [34–36]. Regarding the Oligocene-Early Miocene Suez rifting, the tectonic stages can be categorized into pre-rift, syn-rift, and perhaps post-rift stages (Figure 2). The pre-rift stage was characterized by quiescence in most parts. However, Younes and McClay [37] concluded that the lithological and structural properties of the basement played various roles in rifting, in which basement rocks influenced the quality and volume of clastic material delivered to the Neogene basin as well as the Clysmic and Duwi trends inherited from basement structural discontinuities. With the opening of the Neo –Thethys during the Mesozoic era, as well as the absence of Triassic sediments in the Gulf of Suez area, Patton et al. [38] argued that the northern Gulf of Suez experienced extension and tectonic subsidence during the Lower and

 doi:10.20944/preprints202604.1026.v1

Middle Jurassic. There was also a renewed uplift movement during the Late Jurassic – Early Cretaceous. The absence of substantial doming prior to the Suez rift was disputed by the preservation of the pre-rift sequence. The syn-rift stage was characterized by the intensive tectonic activities that resulted in the subsidence of the basin and the uplift of the shoulders. This allowed for thick deposits to occur, especially in the depocenters. The subsidence rate reached its peak during the deposition of the Lower –Middle Rudeis Formation. According to Bosence et al. [39], fault-block rotation acts as an important control on platform morphology, facies associations, and the development of depositional sequences. They stated that carbonate platforms commonly develop on fault blocks in the late syn-rift to post-rift stage of basin evolution. Montenat et al. [34] argued that all fault trends have a large vertical throw. This means that the former tilt blocks are split into a mosaic of smaller blocks, with carbonates and reefs on the crests and muds on the grabens. During the Late Miocene, the deposition of a thick evaporite sequence was stimulated by the transition of environmental conditions from open marine to restricted ones. Deformation of the Plio – Pleistocene deposits as a consequence of the South Gharib salt movement is the most important tectonic event during the post-rift stage, especially at the southern Gulf of Suez. This movement led to the formation of salt diapers at the central axis of the rift, which were ultimately reduced to salt pillows toward the gulf margins. The salt diapirs functioned as an effective seal for hydrocarbons.

Structurally, the GOS is dominated by normal faults and tilted fault blocks, which were formed during the Miocene [40]. The GOS was divided into three provinces separated by two accommodation zones [41]. The northern and southern provinces are characterized by southwest dip blocks and northeast dip faults and the central province is dominated with northeast dip blocks and southwest dip faults.

Four major fault trends were identified in the Gulf of Suez [34,38]. These are the Clysmic trend NW – SE, N- oblique or Aqaba trend NNE – SSW, NW – oblique or Duwi trend N100 – 120 and cross or transverse fault WSW – ENE. The Aqaba and Duwi trends are oblique to the Clysmic trend. The association of these trends resulted in zigzag fault pattern.

Based on the volume of production, EGPC [42] classified the GOS reservoirs into primary reservoirs such as Middle Miocene Kareem reservoir and Nubia sandstone, secondary reservoirs such as the upper Cretaceous Nezzazat Group, and the tertiary reservoirs such as the fractured basement. The GOS reservoirs are sourced primary from the Campain Duwi Formation and other shale intervals in Eocene, Paleocene, and Miocene. The trapping mechanism is mostly a combination between structural trap and stratigraphic trap. Sealing can be provided by several ways such as juxtaposition of permeable strata against impermeable strata, shale layers, evaporites layers, or salt diapirs.

3. Data and Methods

The dataset utilized in this study was derived from two boreholes (well A and well B) located in the southern GOS, Egypt. The wells are produced hydrocarbon from the encountered Nubia interval. In well A well, the hydrocarbon density can be detected using repeat formation tester (RFT) results, which indicate the presence of three types. The fluid gradient ranges from 0.334 to 0.584 g/cc and the pressure gradient ranges from 0.144 psi/ft (indicating gas) and from 0.28 to 0.25 psi/ft (indicating light oil). According to RFT data of well A, the GOC (gas-oil contact) was located at nearly 10780 ft measured depth, with no OWC (oil-water contact). Another change in fluid density was occurred at about 11000 ft depth. The studied wells are producing hydrocarbon from the Nubia interval. The dataset includes geophysical electric well logs, routine core analysis (RCAL), and special core analysis (SCAL). The electric geophysical logs include gamma ray (GR), density (RHOB), neutron (NPHI), sonic (DT), and true formation resistivity (R_t). One well, well A, includes U, Th, and K natural gamma ray readings. The RCAL data include horizontal and vertical permeabilities, helium and fluid porosities, grain density, and water and hydrocarbon saturations, besides a sedimentological description of the core lithofacies. For well A, the cored interval is about 600 ft thick covered the whole drilled Nubia section except the upper 150 ft, representing about 85% of whole Nubia section

 doi:10.20944/preprints202604.1026.v1

in this well. On the other hand, in well B, the cored interval is about 180 ft thick covering the middle part of the encountered interval. The cored interval represented about 50% of the encountered section. The statistics of the core analyses are presented in Table 1. The SCAL data include measurements of formation resistivity factor (F) and formation resistivity index (n). These measurements are crucial in accurate determination of water saturation (S_w).

Table 1. The statistical summary of the petrophysical parameters of the studied wells.

Well	No. of sample	Permeability, md						
		St.dev.	Min.	Max.	k_A	k_H	k_G	k_A/k_H
A	519	126.65	0.01	1050	68.08	0.413	10.93	164.8
B	155	352.2	0.07	1568	422	3.27	207.71	129.16
total	674							
		Helium porosity						
		St.dev.		Min.		Max.	Averg.	
A	536	3.39		0.016		0.21	0.133	
B	158	2.29		0.08		0.24	0.162	
Total	694							
		FZI, um						
A	519	2.12		0.12		11.47	2.79	
B	155	3.29		0.34		15.98	7.1	
Total	674							
		RQI, um						
A	519	0.433		0.011		2.43	0.48	
B	155	0.63		0.03		3.09	1.41	
Total	674							

St.dev. = standard deviation, k_A= arithmetic mean, k_H= harmonic mean, k_G= geometric mean.

Before dealing with the logs data, environmental correction and depth matching must be carried out first. Standardization and normalization can be used to overcome the variations in vertical logs resolution and depth of investigation. The depth matching between logs and core permeability is the second step. In this step, we used a vertical plot between core k and gamma ray log or density log to compare them (Figure 3). In this study, the logging data were used as raw logs data, were minimized the effect of different scales and units of the logging data using principal component analysis (PCA), and were normalized using the cumulative distribution function (CDF), as illustrated in the following equation:

$$F(x) = \text{norm.dist}(x; u; \sigma; \text{true}) \quad (1)$$

where (x) represents the accumulated probability up to a specific point, x is the random variable, u is the mean, and σ is the standard deviation.

It's common for well logs (e.g., GR, RHOB, etc.) to have skewed distributions. Thus, the results will be biased when raw well logs data are input into clustering algorithms. Subsequently, the cumulative distribution function (CDF) was implemented, which involves the conversion of each log value to a cumulative probability between 0 and 1. Another method to overcome the biased distribution of well log values is PCA. The PCA is applied to normalize and standardize well log data. The output data are presented by PC1, PC2, etc. In order to identify the optimal number of RRT, most representative principal components were chosen as input data for the cluster analysis. In PCA, DT, RHOB, GR, NPHI, and ILD were used as input data. The results were PC1, PC2, PC3, PC4, and

 doi:10.20944/preprints202604.1026.v1

PC5. Training PCA showed that the first three PCs account for 89% of data variability. These PCs reveal that the first PC (PCI) reveals good correlation with RHOB, the second PC (PC2) highly correlates with DT and NPHI, and the third PC (PC3) exhibits a better correlation with GR than the first two PCs (Figure 4). The first three PCs transformations have the following equations:

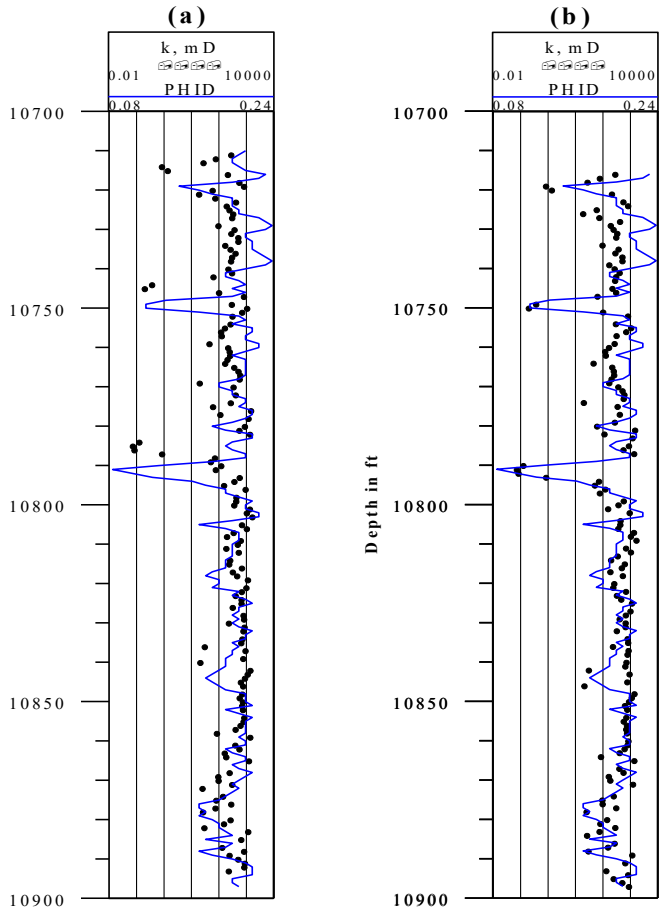

Figure 3. Depth matching using porosity of density log (PHID) and horizontal permeability (k) in well B. a) before depth matching, b) after depth matching.

 doi:10.20944/preprints202604.1026.v1

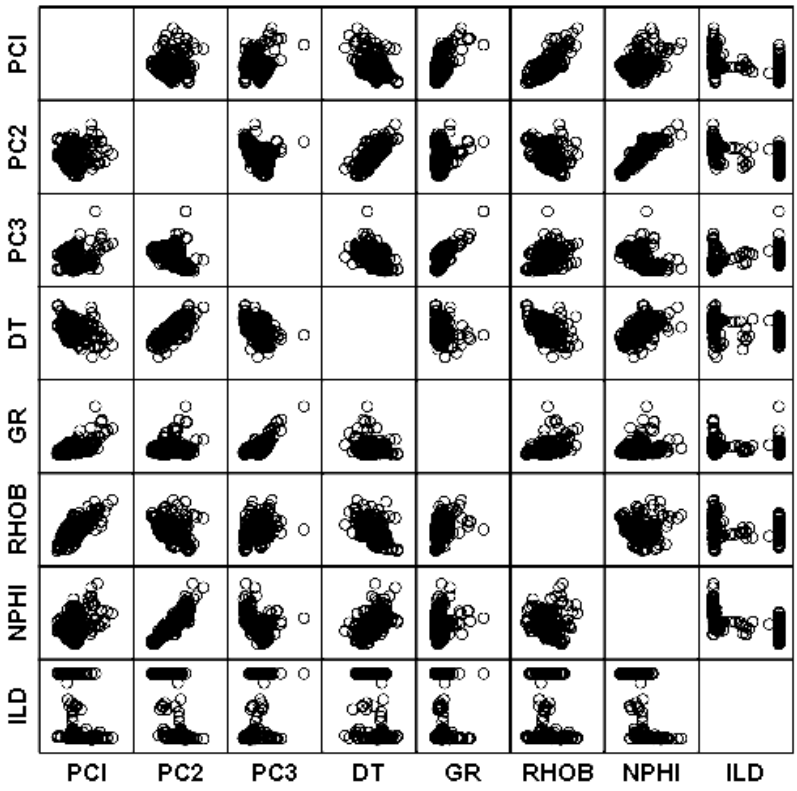

Figure 4. Matrix scatter plot of PC analysis for well B, showing a good correlation between PC1 and RHOB and PC2 and NPHI.

$$PC1=-0.4146(DT)+0.39201(GR)+0.57816(RHOB)+0.29701(NPHI)-0.50195\ (ILD)$$

$$PC2=0.5942(DT)+0.33054(GR)-0.3107(RHOB)+0.6282(NPHI)-0.21962\ (ILD)$$

$$PC3=-0.02895(DT)+0.79028(GR)+0.0385(RHOB)-0.16405(NPHI)+0.5884\ (ILD)$$

The following methods were used to predict the RRT:
Buckles [10], at the irreducible water saturation, introduced the following equation:

$$BVW=S_{wir}*\phi \quad (2)$$

Each RRT has a constant value of BVW.
Based on capillary pressure, R_{35} equation (Winland Equation) was used:

$$\text{Log } R_{35} = 0.732 + 0.588 \log k - 0.864 \log \phi \quad (3)$$

where R_{35} is the pore aperture radius corresponding to the 35th percentile of mercury saturation in micron, k is permeability in mD and ϕ is porosity in percentage**.** The core samples of a given petrophysical flow unit have similar R_{35} values which are used to define HFU as the following:

- Megaport units with $R_{35} > 10$ μm
- Macroport units with $2 < R_{35} < 10$
- Mesoport units with $0.5 < R_{35} < 2$
- Microport units with $0.1 < R_{35} < 0.5$
- Nanoport units with $R_{35} < 0.1$

Stratigraphic modified Lorenz (SML) plot was used to detect the inflection which defines a new RRT. It is a plot of cumulative flow capacity versus cumulative storage capacity. It can be calculated using the following equations:

 doi:10.20944/preprints202604.1026.v1

$$(k_h)cum = k_1(h_1-h_0) + k_2(h_2-h_1) + \ldots\ldots\ldots\ldots + k_n(h_n-h_{n-1}) \quad (4)$$

where k is permeability (mD) and is thickness of the sample interval.

A similar equation is used to determine a single cumulative storage capacity value:

$$(\phi_h)cum = \phi_1(h_1-h_0) + \phi_2(h_2-h_1) + \ldots\ldots\ldots\ldots + \phi_n(h_n-h_{n-1}) \quad (5)$$

where ϕ is fractional porosity.

Determination of hydraulic flow unit (HFU) based on flow zone indicator (FZI), and reservoir quality index (RQI) can be carried out using the following equations [12]:

$$FZI = \frac{1}{\sqrt{Fs}\tau Sgv} = \frac{RQI}{\phi z} \quad (6)$$

In which;

$$RQI = 0.0314\sqrt{\frac{k}{\phi}} \quad (7)$$

$$\emptyset_z = \frac{\emptyset}{(1-\emptyset)} \quad (8)$$

The FZI model can be converted to 3D discrete rock type (DRT) by using the following equation [43]:

$$DRT = round\ (2\log\ (FZI) + 10.7) \quad (9)$$

In this study, three machine learning methods were used to predict the possible RRT in the Nubia sandstone in the southern Gulf of Suez. These methods are:

1- Ward's hierarchical clustering method:

In this method, core k, core ϕ, FZI, ϕ_z, and RQI were used as input data. While, the other two ML methods, well logging data were used as input data. Therefore, the Ward's method can be used as a calibration tool, by which the accuracy of the prediction method can be adjusted. Ward's method is a criterion applied in the unsupervised hierarchical cluster analysis. This agglomerative hierarchical clustering unsupervised learning method is predicated on the organization of the data into a nested sequence of clusters, which in turn forms a dendrogram, a tree-like structure. In Ward's method, the optimal value of an objective function is used to determine the pair of clusters to merge at each step. The first step of the procedure is to calculate a distance matrix that measures pairwise dissimilarities between every data point. The two clusters with the smallest dissimilarity are merged at each iteration. Using linkage criteria, the dissimilarity between clusters can be determined. The linkage criteria could be single linkage (minimum distance), complete linkage (maximum distance), and average linkage (mean distance). A common way to measure dissimilarity is the Euclidean distance, according to the following equation:

$$d(x,y) = \sqrt{\sum_{i=1}^{n}(x_i - y_i)^2} \quad (11)$$

where x and y are two data points in n-dimensional space.

To validate the optimal number of RRT, we plot SSE against the number of HFUs in which the SSE decreased as HFU increased. At a certain HFU number, the SSE is nearly constant. After this certain number, SSE is almost constant with small variations, which can be neglected. This certain number can be considered the optimum number of HFUs.

2. - K-means clustering:

The K-means clustering algorithm is a commonly used unsupervised learning technique designed to partition a dataset into k clusters, where k is a predetermined number. The algorithm goal's is to minimize the within-cluster sum of squared errors (SSE), which gauges how compact a cluster is [44]. Based on the relationships among the variables, the K-means clustering permits the identification of natural groupings or patterns within the data. The SSE can be determined using the following equation:

 doi:10.20944/preprints202604.1026.v1

SSE= $\sum_{k=1}^{K}\sum_{x\in Ck}\|x-\mu k\|^2$ (10)

where Ck represents the set of points in cluster k, μk is the centroid of cluster k, and $\|x-\mu k\|^2$ denotes the Euclidean distance between a point x and the cluster centroid μk.

According to Bradley and Fayyad [45] and Amosu et al. [29], K-means has notable limitations, such as the sensitive to the choice of initial centroids, the sensitive to the outliers, and the assumption of spherical clusters and equal cluster sizes. These limitations can result in a significant distortion of centroid positions.

3- Self-Organizing Maps (SOM)

Self-organizing maps (SOM) is an unsupervised machine learning technique used to produce a low-dimensional (typically two-dimensional) representation of a higher-dimensional data set while preserving the topological structure of the data. For example, a data set with p variables measured in n observations could be represented as clusters of observations with similar values for the variables. These clusters then could be visualized as a two-dimensional "map" such that observations in proximal clusters have more similar values than observations in distal clusters. This can make high-dimensional data easier to visualize and analyze. Self-organizing maps, like most artificial neural networks, operate in two modes: training and mapping. First, training uses an input data set to generate a lower-dimensional representation of the input data. Second, mapping classifies additional input data using the generated map.

4. Results and Discussion

The tilted fault blocks, which characterized the Suez rift, resulted in a considerable variation in the thickness of encountered drilled intervals, such as the Nubia interval in the studied wells. The thickness varies from about 700 ft thick in the well A to about 360 ft thick in well B. This variation in thickness is attributed to fault-cutting rather than a non-deposition or erosion process. Using well-to-well correlation confirmed this interpretation, in which the upper part of the Nubia interval was encountered in well B, while the lower interval is missing (Figure 5). The correlation between the two wells was carried out using GR and DT logs. However, resistivity log provides a valuable assistance in this correlation. As indicated from the dip log (Figure 5), the Nubia interval is rested unconformably on the basement rock and overlain unconformably by Upper Cretaceous Matulla Formation. Moreover, unconformity surfaces can be detected between different lithofacies of the Nubia sandstone.

 doi:10.20944/preprints202604.1026.v1

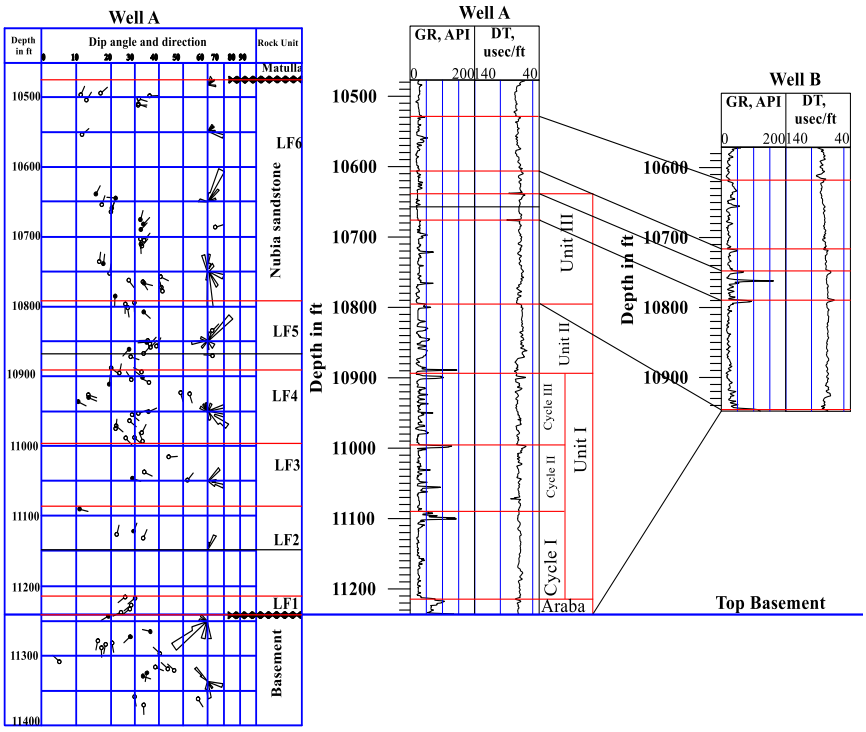

Figure 5. Well-to-well correlation between well A and well B, showing the missing the lower part of Nubia sandstone in well B probably due to fault-cutting. The dipmeter log of well A shows possible unconformity surfaces separated the lower three lithofacies.

4.1. Lithofacies Based on Core Description:

Well A cores of presented a good opportunity to identify and characterize the lithofacies of the Nubia sandstone. The cores revealed that the Nubia interval consists of three lithologies, which are sandstones (main constituents), conglomerates, and shales (minor constituents). Moreover, the cored interval in well A (about 600 ft thick) revealed seven different lithofacies:

4.1.1. Dark Grey to Black Quartzarenite Lithofacies (LF1)

This lithofacies represented the lowermost interval of the Nubia sandstone and attained a thickness of about 25 ft. It is deposited on the fractured basement and is characterized by high GR readings as a result of the presence of radioactive minerals (Figure 6). According to Gameel and Darwish [31], the lower 2.5 ft is composed of thick black sandstone with basalt granules, cemented by silica, and plugged by clay minerals, indicating a deposition in shallow marine conditions. The upper part is composed of light tan, very fine to fine grains, medium-sorted, and cemented by kaolinite. LF1 is characterized by an average porosity of 13.6%, poor permeability of an average of 0.68 mD, and an average true formation resistivity of 5.3 ohm.m. This lithofacies shows a poor relationship between ϕ and k, with $r^2 = 0.02$ (Figure 7). This suggested that the authigenic clay minerals plug the relatively high porosity ($\phi_{avg.}$ = 13.6%) and as a result, the porosity has no discernible impact on the permeability values.

 doi:10.20944/preprints202604.1026.v1

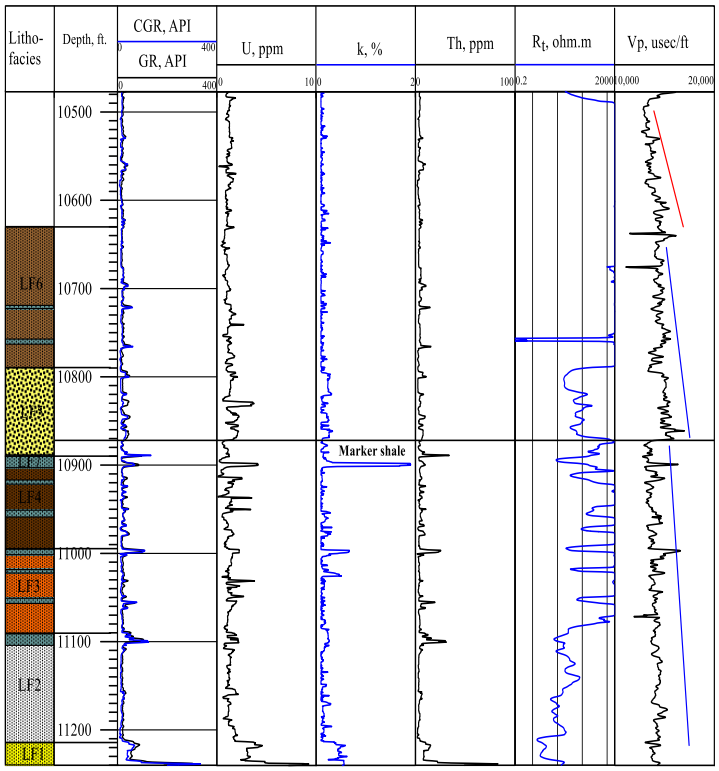

Figure 6. Crossplot of radioactive minerals (U, Th, and K) in well A.

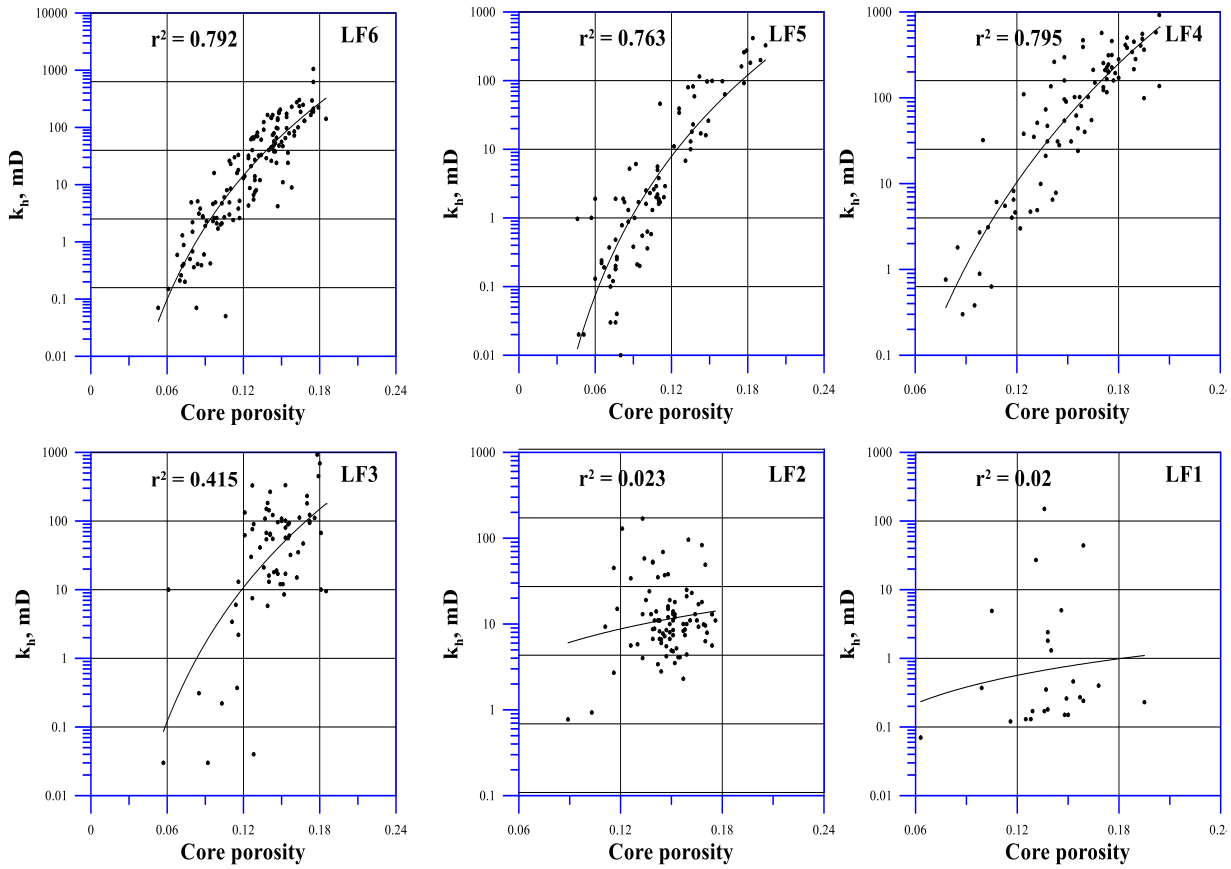

Figure 7. Crossplots of core permeability versus core porosity for the different lithofacies in well B. Best correlation was for LF6 and the worst correlation was for LF1.

 doi:10.20944/preprints202604.1026.v1

4.1.2. Black Colored Coarse Pebbly Sandstone Lithofacies (LF2)

This lithofacies represented a basin floor fan, as indicated by the GR curve. It attains about 100 ft thick. It is capped by a thin layer of shale. LF2 seems to be dissected into two units. The lower unit has R_t around 10 ohm.m and the upper unit has R_t between 10 and 100 ohm.m (Figure 6). This variation in resistivity log response can also be observed in both GR and DT logs. LF2 is composed of dark brown to dark tan, fine to medium grains, occasionally coarse grains, medium-sorted, and cemented. The average porosity is 14.7%, and the average permeability is 18.8 mD. The relationship between k and ϕ is very poor, recoding $r^2 = 0.023$. According to Gameel and Darwish [31], the geochemical reaction between pyritic sulfur content and the hydrocarbons led to the formation of pyrobitumen, which fills the pore space.

4.1.3. Brown Pebbly Sandstone Lithofacies (LF3)

This lithofacies shows coarsening upward as indicated by the GR curve. Resistivity log gives high (R_t >1000 ohm.m), except for two thin zones, in which R_t decreases to less than 100 ohm.m. These two zones are corresponding to shale layers (Figure 6). LF3 is composed of dark tan, fine to medium to coarse grains, medium to well-sorted, medium to well-cemented, argillaceous in parts, and pebbly in parts. It is capped with a thin layer of shale. The porosity and permeability recorded average values of 14.4 and 96.3 mD respectively. The porosity–permeability shows weak relationship, with $r^2 = 0.415$.

4.1.4. Brown Sandstone Lithofacies (LF4)

This lithofacies is embraced between two layers of shales. The lower shale layer is very fine grained siltstone with possible dolomite cement. The upper shale layer is called “marker shale”, which can be easily correlated within the Nubia interval in other wells. The highest potassium readings were recorded within this marker shale (Figure 7). The sandstone is light to dark tan, fine- to medium-grains, medium-sorted, subangular, subrounded, and medium to well-cemented. The resistivity log shows zones with R_t > 1000 ohm.m intercalated with zones with R_t < 100 ohm.m. Porosity and permeability recorded average values of 15.3% and 165.3 mD, respectively. Contrary to the preceding lithofacies, the porosity–permeability relationship of this lithofacies exhibits a positive correlation, with $r^2 = 0.795$ (Figure 7). According to Gameel and Darwish [31], the last three lithofacies (LF2-LF4) were deposited in distributary channels and bars.

4.1.5. Conglomeratic to Argillaceous Sandstone Lithofacies (LF5)

This lithofacies shows specific character for both resistivity and sonic logs.The resistivity values are around 100 ohm.m, with no extreme high R_t values as in LF3 and LF4. The sandstone is light tan to dark brown, medium–fine grains, occasionally very fine, occasionally coarse, fair to poorly-sorted, pebbly in parts, with traces of pyrite, and with siliceous cement. Porosity and permeability recorded average values of 10.7% and 34.6 mD, respectively. The porosity–permeability relationship of this lithofacies shows the best correlation among the studied lithofacies, with $r^2 = 0.763$ (Figure 7). LF5 may be deposited under coastal conditions.

4.1.6. Siliceous and Argillaceous Sandstone Lithofacies (LF6)

This lithofacies represented the uppermost part of the Nubia interval. LF6 has a potential to be deposited under aeolian conditions. LF6 is characterized by a high R_t >1000 ohm.m. The radioactive plot shows no normal readings for all the radioactive minerals (Figure 6). It attains the thickest interval. When combined with the uncored interval; its thickness reaches approximately 350 ft. The sandstone is brown to dark brown, medium to coarse grains, semi – friable, with siliceous cement, fair to poorly-sorted, occasionally well-sorted, and occasionally with pebble grains. Porosity and permeability recorded average values of 12.5% and 67.4 mD, respectively. The porosity–permeability relationship of this lithofacies shows a good correlation, with r^2 =0.792 (Figure 7).

 doi:10.20944/preprints202604.1026.v1

4.1.7. Shales (LF7)

Shales occurred as thin streak layers throughout the Nubia interval. Shales can be observed at a depth of 11000 ft, between 11091 and 11003, and between 10892 and 10902 (Figure 6). Illite and pyrite are the dominant clay minerals between 10892 and 10902 ft depth, while cryptocrystalline amorphous silica is encountered at 10918 and 11000 ft depth. Generally, the dominant clay minerals are kaolinite and illite.

4.2. Porosity–Permeability Relationship

Tiab and Donldson [46] classified the reservoir quality into five categories according to the permeability values:

Poor reservoir: k< 1mD

Fair reservoir: 1<k<10 mD

Moderate reservoir: 10<k>50 mD

Good reservoir: 50<k>250 mD

Very good reservoir: k>250 mD.

Figure 8 shows that LF1 is mostly poor reservoir rock type, while LF2 is the only lithofacies that has no poor reservoir rock type. It is mostly fair and moderate RRT. LF3 shows increasing the reservoir quality upward, while LF4 shows high percentage of very good RRT. In contrast with LF3, LF5 shows decreasing of reservoir quality upward. LF6 is mostly ranged from fair to good RRT.

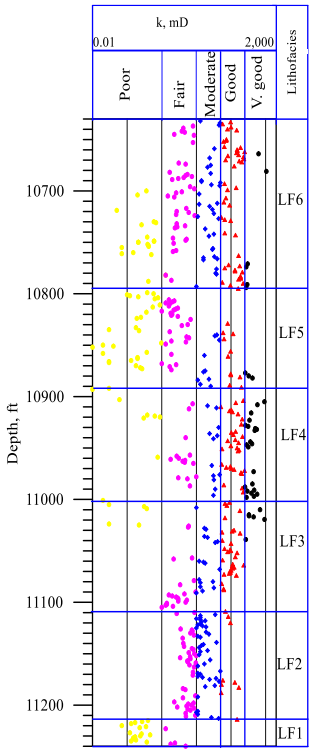

Figure 8. Showing the classification of the Nubia sandstone into reservoir rock quality in well A.

The core analysis provides two types of porosities: helium porosity (ϕ_h) and fluid porosity (ϕ_f). The relationship between the two porosities is moderate, with $r^2 = 0.609$. The most robust correlation was observed in LF5, which recorded $r^2 = 0.82$. For the lowermost three lithofacies (LF1-LF3), the helium core porosity values are mostly restricted between 12 and 18% (Figure 9). Meanwhile, the helium core porosity values of the uppermost three lithofacies show primarily limited to the range of 6 to 18%, with noticeable variations in LF4, where ϕ > 18% is recorded. There is no discernible downward trend in the porosity with depth, except for the uppermost two lithofacies where a general downward trend in the porosity with depth can be observed (Figure 9). The magnitude of k in the

 doi:10.20944/preprints202604.1026.v1

uppermost three lithofacies is a reflection of the variation in porosity values, suggesting that porosity is the primary factor influencing k values. As noted in Figure 8, a change in ϕ corresponds to a change in k. The relationship between k and ϕ in these three lithofacies shows r^2 ranged between 0.494 and 0.664. On the other hand, the lowermost three lithofacies (LF4-LF6) show no or low matching between k and ϕ. The relationship between k and ϕ in these three lower lithofacies shows r^2 that falls within a range of 0.011 to 0.331. This means that other factors rather than porosity are playing the main role in determining the magnitude of k.

The total porosity–derived log gives a better correlation with helium core porosity than fluid core porosity, with $r^2 = 0.541$. Therefore, the helium core porosity is a better representation of the actual formation porosity than the fluid porosity. The complicated heterogeneous nature of the reservoir of well A results in a moderate relationship between log and core porosities. In well B, a good relationship between core and log-derived porosity was observed (Figure 10). The porosity of well B is mostly restricted between 12 and 18%. Some variations can be observed in the upper interval, in which ϕ>18% is recorded. It appears that the porosity curve is characterized by alternating crescents.

The relationship between horizontal permeability (k_h) and core porosity is moderate for the whole interval of well A, with $r^2 = 0.55$, but it increases in well B to 0.602. In the case of vertical permeability (k_v), the relationship between k_v and ϕ got weaker, with $r^2 = 0.45$ for well A and 0.473 for well B. The relationship between k_h and k_v can be expressed using the following equation, with $r^2 = 0.732$:

$$k_v = 0.959 * k_h^{0.824} \quad (12)$$

 doi:10.20944/preprints202604.1026.v1

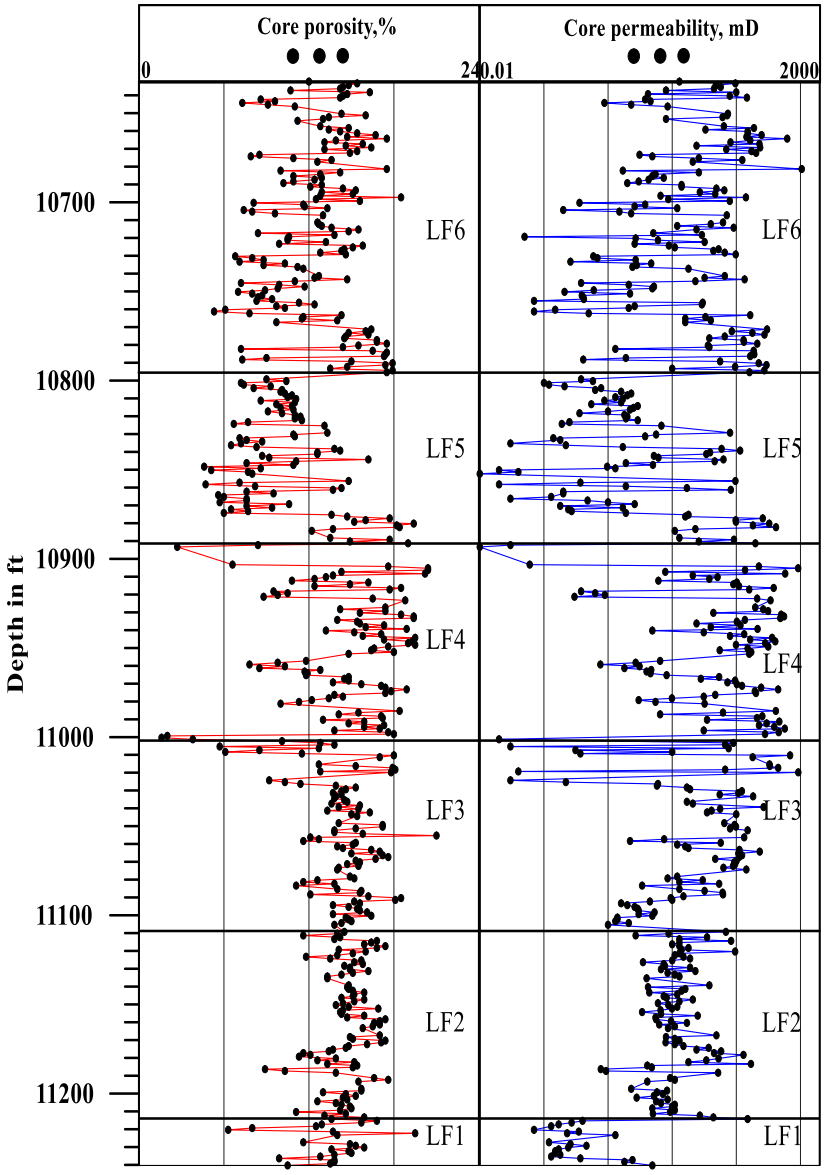

Figure 9. Crossplot of core permeability and core porosity in well A, showing that the magnitude of permeability is a reflection of the magnitude of porosity except for LF1 and most of LF2, which explain the poor correlation between k and ϕ in these two lithofacies.

Incorporating porosity in the form of $\sqrt{\frac{k_h}{\emptyset}}$ or $\sqrt{k_h * \emptyset}$ yielded no strength in the relationships between k_v and k_h. The coefficient of determination was lowered to 0.713 and 0.729, respectively. In well B, a significant drop in r^2 was noted from 0.823 to 0.777 when incorporating porosity in Eq. 12. This may suggest that porosity has a limited impact on the magnitude of k. The relationship between k_h and ϕ based on reservoir quality (poor, fair, etc.) reveals very poor relationships with r^2 ranging from 0.076 to 0.247. The porosity – permeability relationship seems to interpret in the light of the Nelson [47] plot. According to this plot, the cementation and clay content are primary influence parameters in the reduction of k. Both have a negative impact on the k values. The response varies from one lithofacies to another. For example, LF6 shows an obvious trend between k and phi as a result of the increase in cementation, consolidation, diagenesis, and clay contents (Figure 10). Conversely, LF2 doesn't exhibit this trend, as a significant decrease in k was not accompanied by a comparable increase in ϕ (Figure 10). In well B, on the other hand, the reservoir characteristics were enhanced through low cement, low clay content, and increase in grain size and degree of sorting, which led to high k and ϕ (Figure 10).

 doi:10.20944/preprints202604.1026.v1

4.3. Traditional Methods for RRT

Buckles plot introduced a method by which RRT can be differentiated. Figure 11 shows several rock types that can be detected in well A. Only LF6 gives one rock type, with C = 0.004, indicating good reservoir quality. On the other hand, LF2 has a wide range of C, extending between C = 0.02 and 0.06. Unlike the other lithofacies, LF2 shows a limited variation in porosity. LF3 shows a wide range of variation in both S_w and ϕ, with one cluster around C = 0.004. High reservoir quality can be found in LF6 and parts in LF3 and LF4. On the other hand, poor reservoir quality is restricted in LF1, while low reservoir quality can be detected in LF2 and LF5. In well B, one cluster around C = 0.002 can be detected, representing the bulk encountered Nubia interval in this well.

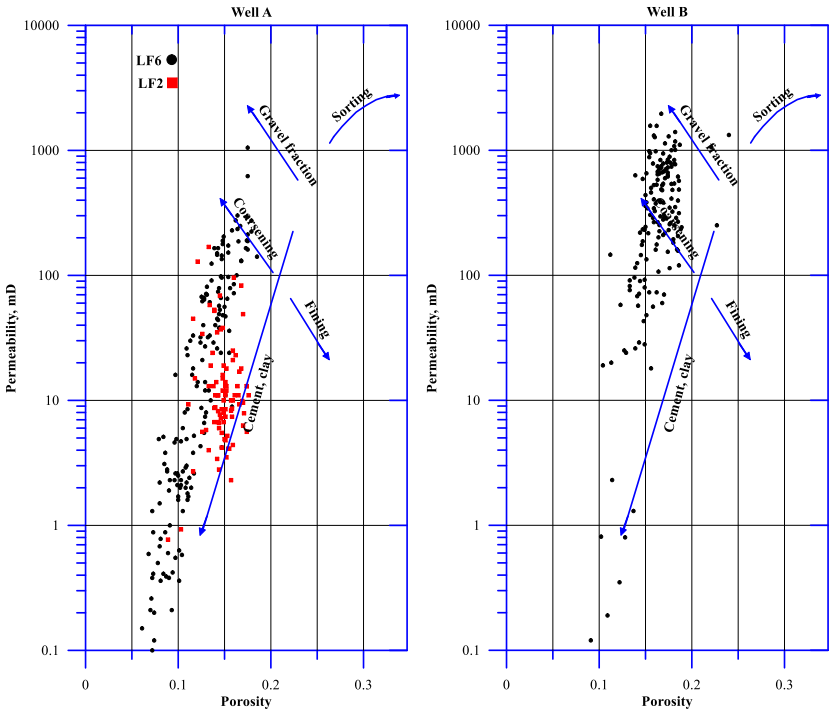

Figure 10. Showing the effect of cementation on the magnitude of the permeability in well A, while well B is characterized by coarse grain sizes and low effect of cementation, which resulted in good to very good reservoir quality (adopted after [47]). .

 doi:10.20944/preprints202604.1026.v1

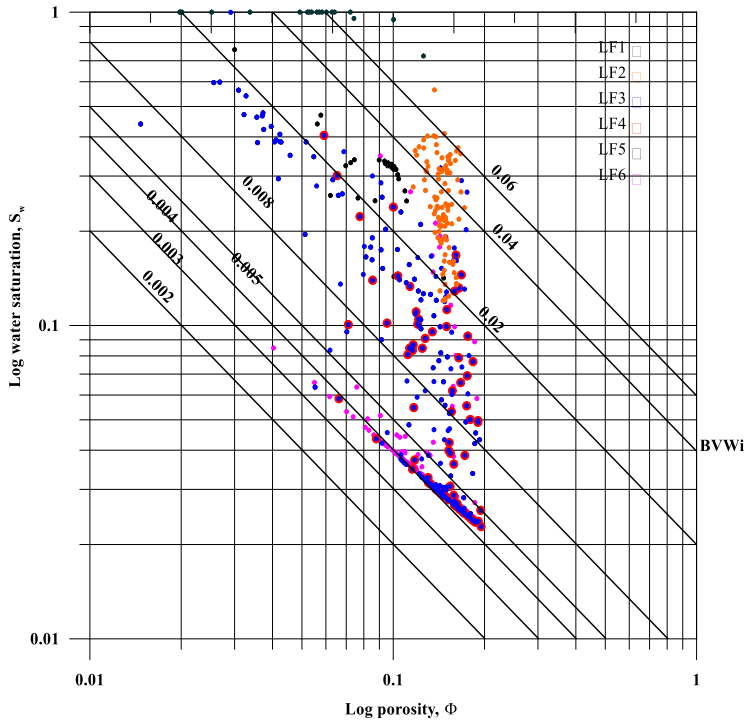

Figure 11. Buckles plot of the Nubia sandstone of well A.

Using the R_{35} equation, well A displays five RRT. LF6 and LF5 are extended throughout the five categories, with an obvious proportional trend between k and ϕ (Figure 12). LF4 shows mostly macro and mega rock types, with an obvious proportional trend between k and ϕ. The majority of LF3 is composed of macro and mega rock types, with no discernible trend between k and ϕ. For LF3, it can be noted that increasing k is not associated with increasing ϕ. LF2 is predominantly macro rock type, the relationship between k and ϕ is absent as is the case in LF3. LF1 is mostly distributed between nano and micro rock types and there is no obvious relationship between k and ϕ. Well B gives a single cluster that falls between mega and macro rock types, with a pore throat size exceeding 5 mm. In this well, there is no obvious trend between k and ϕ, as k rose from 100 to 1000 mD without ϕ changing.

 doi:10.20944/preprints202604.1026.v1

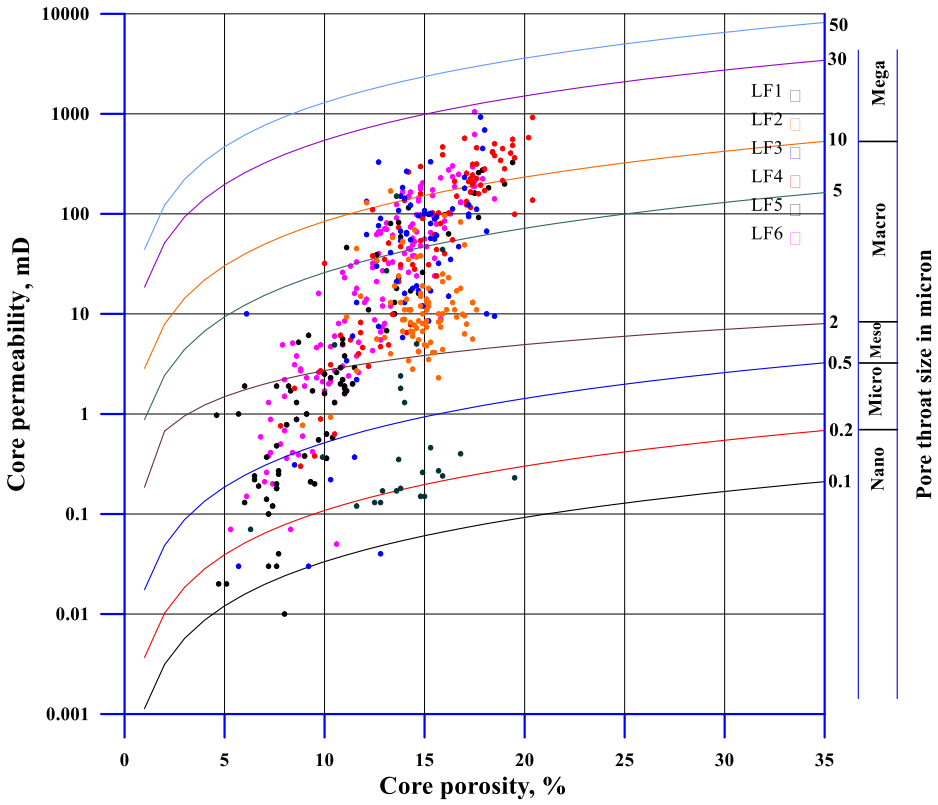

Figure 12. Showing crossplot of k versus ϕ based on Winland equation for well A.

Using porosity as a storage capacity and permeability as a flow capacity, the stratigraphic modified Lorenz (SML) plot provides a simple method for detecting RRT. Eight HFUs can be detected in well A by plotting the storage capacity against flow capacity (Figure 13a). The quality and thickness of the resultant flow units vary from one flow unit to another. While HFU4 represents the lowest reservoir rock quality, HFU3 represents the highest quality among the others, as indicated from the slope of each of them. By using depth as a parameter, it can be inferred that HFU3 was the source of roughly 60% of the flow delivered from the interval between 10880 and 11063 ft depth (Figure 13b). HFU3 corresponds to LF3 and LF4, which dominated by high-quality reservoir and low percentage of low-quality reservoir (Figure 8). For well B, five HFU can be detected using the SML plot (Figure 14a). As in well A, HFU3 represents the thickest and the highest quality reservoir flow unit in this well. In well B, the HFU3 supplied about 60% of the flow. It came from a range depth of 10800 to 10873 ft (Figure 14b).

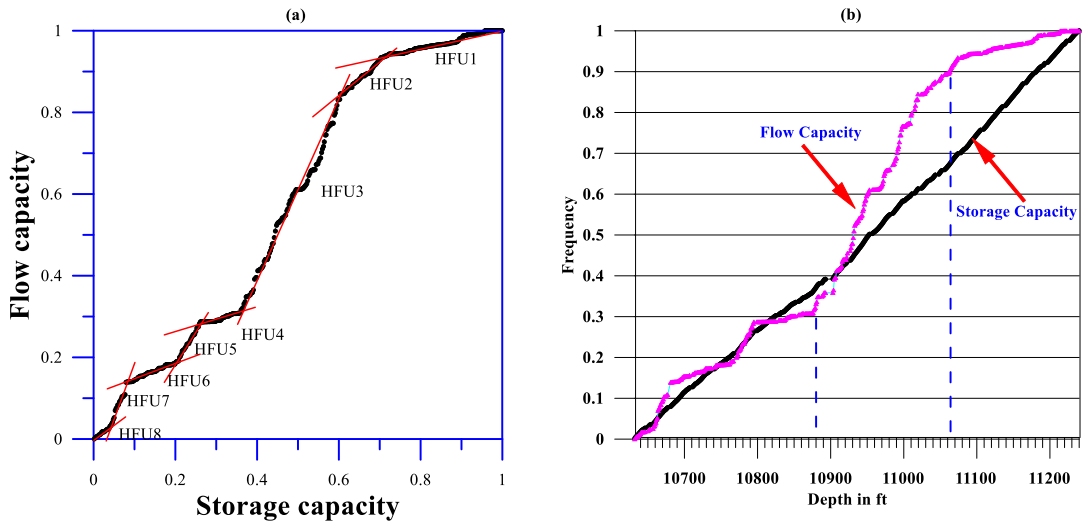

 doi:10.20944/preprints202604.1026.v1

Figure 13. Showing the SLM crossplot for well A, resulting in 8 HFUs (a). Plotting versus depth (b) indicated that the interval between 10880 and 11063 ft depth contributed about 60% of the hydrocarbon in this well. .

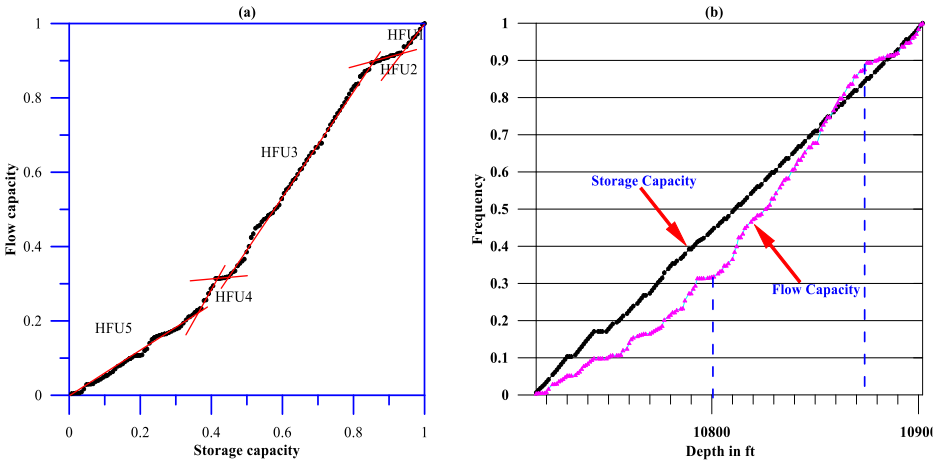

Figure 14. Showing the SLM crossplot for well B, resulting in 5 HFUs (a). Plotting versus depth (b) indicated that the interval between 10800 and 10873 ft depth contributed about 60% of the hydrocarbon in this well. .

Amaefule at al. [12] approach introduced a theoretical attempt by plotting RQI versus ϕ_z, based on Carman-Kozeny equation, to classify the reservoir rocks into HFUs. Figure 15a shows difficulty of accurate determination of HFUs. Their determination depends mostly on manual intervention. The difficulty is a result of the normalized porosity's narrow width. The same behavior can be observed in well B (Figure 15b). The loss of depth information is another drawback of this approach. The use of DRT facilitates the process of determining the slope of lines. In well B, change of the slope of lines throughout different HFUs can be observed (Figure 15b). This change in the slope of lines may be attributed to the impact of the change of cementation factor on HFUs [14]. NRQI (normalized RQI) provides a robust method to achieve the goal of determining HFU. As shown in Figure 16, eleven HFUs can be detected by using NRQI, in which LFI-LF4 correspond to HFU1-HFU4. Meanwhile, LF5 corresponds to HFU6 and HFU7, and the uppermost lithofacies (LF6) corresponds to HFU8-HFU11. As noted from Figure 16, increasing the slope of the plotted NRQI line corresponds to increasing the quality of the rock reservoir. In contrast, a vertical line indicates a rock reservoir of low to poor quality. Therefore, LF1 and LF7 are regarded as having the lowest reservoir rock quality, followed by HF5. In well B, 6 HFUs can be detected in this well (Figure 16). HFU4 and HFU6 can be treated as barriers due to their vertical slope, while HFU3 and HFU5 can be considered the best quality rock type in this well.

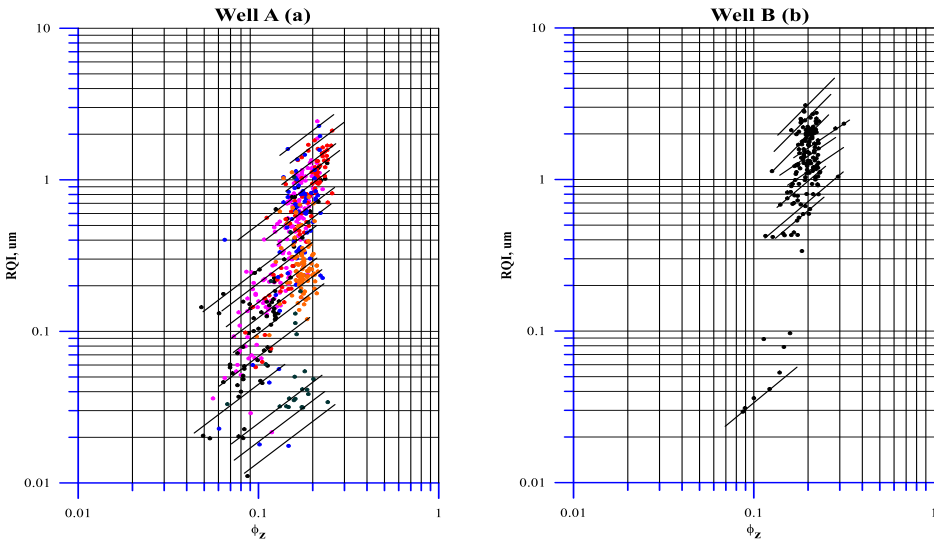

 doi:10.20944/preprints202604.1026.v1

Figure 15. Showing the crossplot of RQI versus ϕz for the two studied wells. The results indicate obvious difficulty in determine the accurate number of HFUs as well as losing the depth.

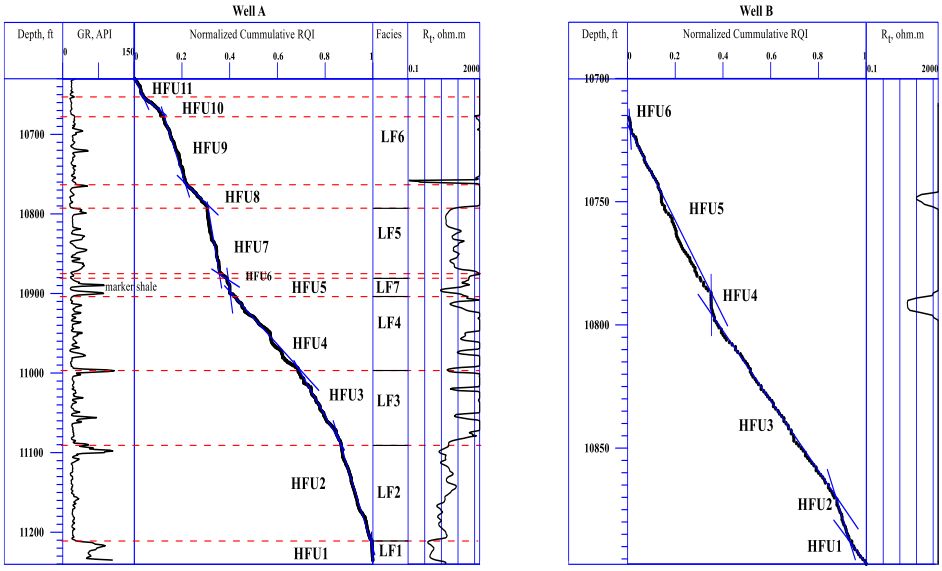

Figure 16. Showing the normalized reservoir quality index versus depth in the two studied wells.

GHE can make it easier to find the number of HFUs based on the FZI approach. Figure 17a shows that the plotted data of well A extended from GHE1 to GHE7. The majority of the points are spread out in GHE4 to GHE6. For well B, the majority of the points fall between GHE6 and GHE7, suggesting high reservoir quality (Figure 17b). The type curve developed by [19] resulted in interference RRT because the lines representing different types of rock have very small gap between them. Therefore, this curve can only be used with limited and wide distribution data. Even though, a more trustworthy approach should be used to adjust the results obtained by [19] type curve.

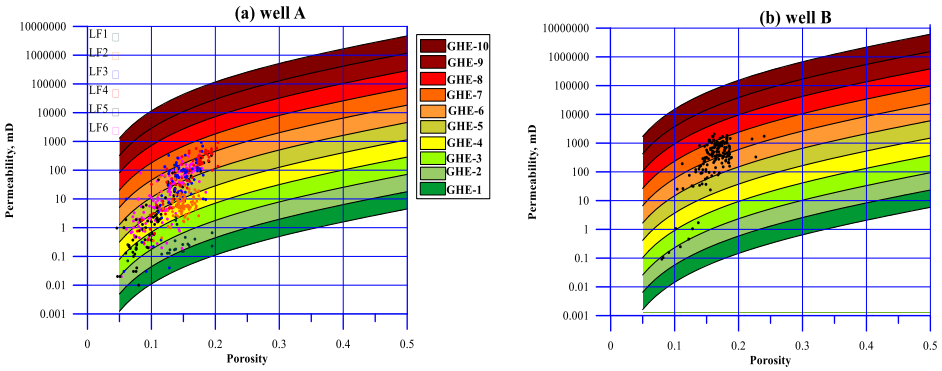

Figure 17. Showing the global hydraulic elements (GHEs) results for the studied two wells.

4.4. Machine Learning (ML) Methods

Ward's hierarchical algorithm provides high accuracy and unlike the FZI approach, it is user-independent. In this method, core k, core phi, ϕz, FZI, and RQI were used as input data. In Ward's method, each data point forms a discrete cluster, and similar clusters are then merged together to form super clusters. A dendrogram is the output of the hierarchical clustering. The sum of square error (SSE) was employed to detect the optimal number of RRT. Eight RRTs, labeled from 1 to 8, can be identified from this method in well A (Figure 18). As the number of RRT increases, the reservoir rock quality decreases. It can be noted that RRT1 and RRT2 are restricted in the very good reservoir rock. On the other hand, good reservoir rock was primarily represented by RRT3, RRT4, and RRT5.

 doi:10.20944/preprints202604.1026.v1

RRT6 is mostly moderate reservoir rock. RR7 is restricted in fair reservoir rock, whereas RR8 is restricted in poor reservoir rock. Some RRTs may experience interference, although this interference is usually minimal. The distribution of RRT1 and RRT2 (good to very good reservoir) represented less 10% of the total cored interval, meanwhile RRT7 and RRT8 (fair to poor reservoir) represented about 45% of the total cored interval. Following the same procedure implemented in well A, six RRTs were identified in well B (Figure 19). In contrast to well A, the poor reservoir quality (RRT6) represents about 6% of the cored Nubia interval in well B. RRT1-RRT4 exhibit very good reservoir quality, accounting for about 80% of the cored interval. Meanwhile, RRT5 shows moderate to good reservoir quality. The merger of the first four RRTs, which represent very good reservoir quality, will result in three principal RRTs that are dominated by very good reservoir rock type with interference of poor and moderate reservoir quality. The correlated section between the two wells (Figure 5) reveals poor to good reservoir rock types in well A and predominately very good reservoir rock type in well B, indicating a significant difference in reservoir quality between the two wells. The correlated section in the two wells is characterized by high true formation resistivity of up to 2000 ohm.m. However, a high-quality reservoir is not guaranteed by this extremely high R_t. This might be explained by the rock texture and post-deposition diagenesis, such as presence of authigenic clay minerals, high viscous asphaltic matter, compaction and development of siliceous overgrowths. While the quartz grains in well A are primarily fine to medium grained and poorly to moderately sorted, the quartz grains in well B are primarily moderate to coarse-grained and moderately to well-sorted.

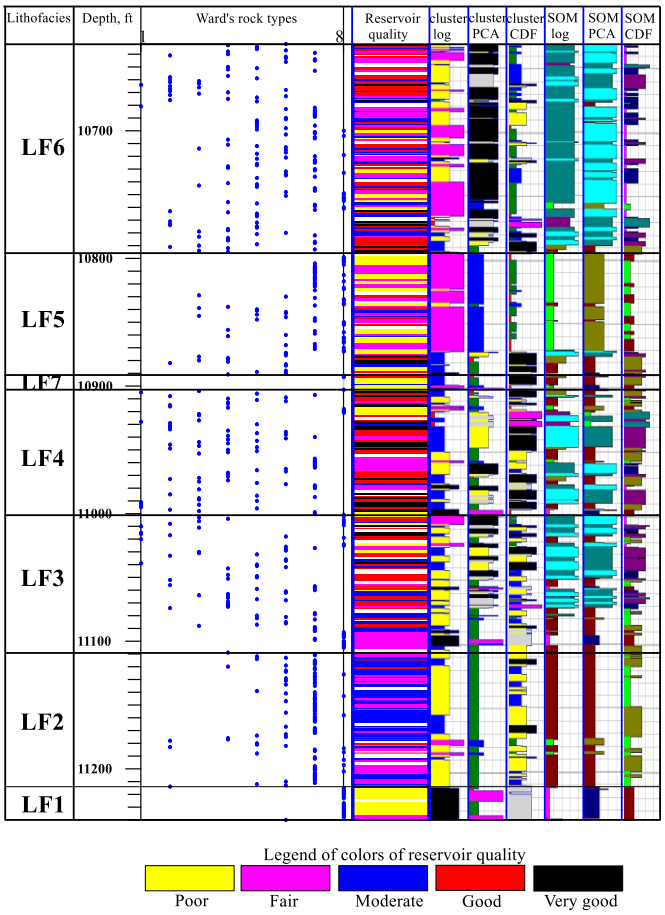

Figure 18. Results of machine learning methods in well A.

 doi:10.20944/preprints202604.1026.v1

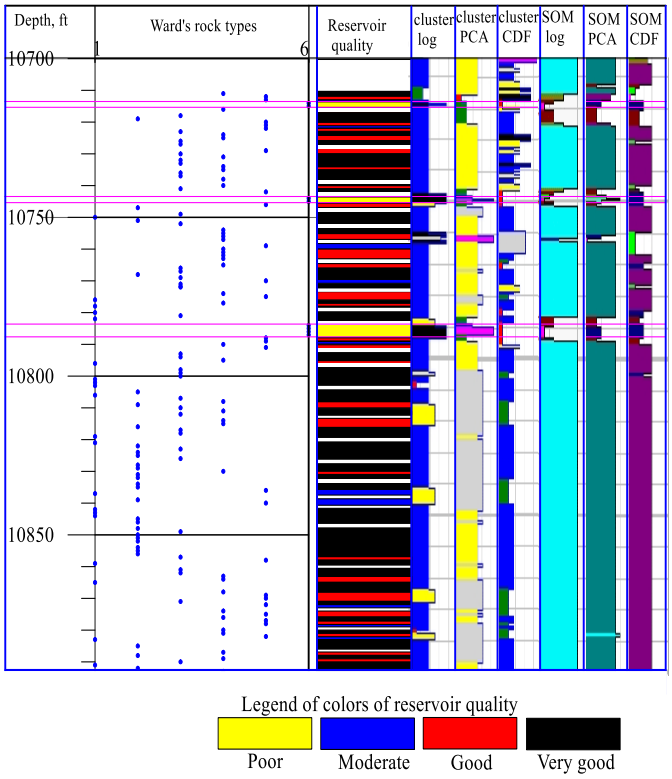

Figure 19. Results of machine learning methods in well B.

Raw logging data, PCs, and CDF were used as input data for K-means clustering and SOM ML methods to verify which one works best. The calibration was determined by the highest degree of a correlation between the results obtained from these input data and the previously identified lithofacies and the category of the reservoir quality (Figs. 18 and 19). The lower lithofacies (LF1) is considered a distinctive one that is not repeated throughout the Nubia interval. It is characterized by very low k and high GR readings. The lowermost 2.5 ft zone of this lithofacies is composed of black thick sandstone that contains basalt granules and has transgressed over the basement. This zone can be differentiated by K- means clustering and SOM methods based on raw logging and PCs as input data. On the other hand, the CDF input data was unable to distinguish this zone (Figure 18). LF2 is characterized by a narrow distribution of porosity and a very weak correlation between k and ϕ. It is mostly composed of an alternation of fair and moderate reservoir quality, with a thin layer of good reservoir rock type. The K-means clustering method based on logs and PCs provided the best translation of this lithofacies distribution. SOM method based on logs and CDF succeeded in predicting of the thin layer of good reservoir quality but it failed to predict the alternation between fair and moderate reservoir quality. LF3 is characterized by the first appearance of very good reservoir quality, with a low percentage of fair and poor reservoir rock types. Based on raw logging data, SOM and K- means clustering methods effectively represented this lithofacies distribution. This lithofacies is characterized by the first appearance of two colors (turquoise and moss green), which represent the good to very good reservoir rock types. Out of all the lithofacies, LF4 shows the strongest correlation between k and ϕ. As in LF3, SOM and k-means clustering methods were conveyed for this lithofacies based on raw logging data. LF5 mainly composed of an alternative for poor and fair reservoir rock types. SOM and K-means clustering methods based CDF effectively differentiated this lithofacies but failed to detect the moderate to good reservoir rock type zones. LF6 is characterized by good correlation between k and ϕ. It is composed of an alternation between various RRTs. The SOM and K- means clustering methods based on raw logs and PCs can give a good presentation for this lithofacies. In conclusion, the rock types of the Nubia sandstone in well A can

 doi:10.20944/preprints202604.1026.v1

be reasonably predicted using SOM and K-means clustering methods based on raw logging data and PCs. However, one of these methods' limitations might be their incapacity to identify the thin zones.

In well B, the Nubia sandstone reservoir can be identified into six RRTs based on the Ward's clustering method (Figure 19). The first four RRTs (1-4) represent very good reservoir quality, which can be merged in one RRT. These rock types represent the bulk interval of the Nubia section in this well, intercalated with some thin layers of poor (RRT6) to good (RRT5) reservoir quality. K-means clustering based on well logs data was the best method to detect the poor quality reservoir rock type (RR6). The remainder of the section was correlated with the high quality rock type (RRT1-RRT4).

5. Conclusions

This study focused on the identification of reservoir rock types (RRTs) in the pre-Cenomanian Nubia sandstone of the Gulf of Suez, Egypt. This Nubia sandstone is regarded as one of the most productive reservoirs in the Gulf of Suez. Using sedimentological core description, routine core analysis, and well logging data of two wells, the results indicate:

1. Fault-cutting is the primary cause of the thickness variation between the two wells under investigation, rather than stratigraphic factors.
2. The cored section in well A can be distinguished into seven distinct lithofacies (LF1-LF7). Six of them are represented by different types of sandstone, and the seventh lithofacies is represented by mudstone.
3. The cored interval in well A is dominated by moderate reservoir rock quality, while the cored interval in well B is dominated by very good reservoir rock quality. This variation may be attributed to the post-deposition diagenesis processes and the variation in sandstone texture.
4. The normalized reservoir quality index (NRQI) method is arguably the most reliable traditional method for predicting the Nubia rock types, especially when it is plotted against depth.
5. The Ward's method, based on core permeability and porosity, resulted in eight RRTs in well A and six RRTs in well B. it is possible to combine the first four RRTs in well B into a single RRT, leaving just three RRTs and dominating by very good reservoir quality.
6. Correlation with Ward's method, the K-means clustering and self-organizing maps (SOM) methods based on raw logging data and principal component analysis (PCA) resulted in the most reliable methods to predict the RRTs in the Nubia sandstone.

Funding: This research received no external funding.

Data Availability Statement: The data that support the findings of this study are available from the Egyptian General Petroleum Corporation (EGPC), but restrictions apply to the availability of these data, which were used under license for the current study, and, therefore, are not publicly available. Data are, however, available from the authors upon reasonable request and with permission from the Egyptian General Petroleum Corporation (EGPC).

Acknowledgments: The author is grateful to the Egyptian General Petroleum Corporation (EGPC) and the Gulf of Suez Petroleum Company (GUPCO) for providing the data.

Conflicts of Interest: The author declares that I have no known competing financial interests of personal relationships that could have appeared to influence the work reported in this paper.

References

1. Gunter, G.; Finneran, J.; Hartmann, D.; Miller, J. Early determination of reservoir flow units using an integrated petrophysical method. *In Proceedings of the SPE Annual Technical Conference and Exhibition, San Antonio, TX, USA, 5–8 October* **1997**; p. 8.
2. Archie, G.E. Introduction to petrophysics of reservoir rocks. AAPG Bull. 1950, 34, 943-961.
3. Michel, R.; Bruno, L. Rock-typing in carbonates: a critical review of clustering methods. SPE 171759 **2014**; p. 15.

 doi:10.20944/preprints202604.1026.v1

4. Rushing, J.A.; Newsham, K.E.; Blasingame, T.A. Rock typing - keys to understanding productivity in tight gas sands. *SPE 114164* **2008**; p. 31.
5. Leverett, M.C. Capillary behavior in porous solids. *Trans. AIME* **1941**, 42, 152-169.
6. Thomeer, J.H.M. Introduction of a pore geometrical factor defined by the capillary pressure curve. *J. Petrol. Tech.* **1960**, 73-77.
7. Winland, H.D. Oil accumulation in response to pore size changes, Weyburn field, Saskatchewan. *Amaco Production Research Report* **1972**, No. F72-G-25.
8. Kolodzie, S.Jr. Analysis of pore throat size and use of the Waxman-Smits equation to determine OOIP in Spindle Field, Colorado. *SPE 9382* **1980**, 55th Annual Fall Technical Conference; p. 10.
9. Pittman, E.D. Relationship of porosity and permeability to various parameters derived from mercury injection-capillary pressure curves for sandstone. *AAPG Bull.* **1992**, 76, 191-198.
10. Buckles, R.S. Correlating and averaging connate water saturation data. *J. Cana. Petrol. Tech.* **1965**, 9, 42-52.
11. Asquith, G.; Gibson, C. Basic well log analysis for geologists. *AAPG* **1982**, Tulsa, OK.
12. Amaefule, J.; Altunbay, M.; Tiab, D.; Kersey, D.; Keelan, D. Enhanced reservoir description using core and log data to identify hydraulic flow units and predict permeability in uncored intervals/wells. *SPE 26436* **1993**, 205-220.
13. Jongkittinarukorn, K.; Tiab, D. Identification of flow units in shaly sand reservoirs. *J. Petrol. Sci. Eng.* **1997**, 17, 237– 246.
14. Nooruddin, H.; Hossain, M.E.; Sudirman, S.; Sulaimani, T. Field application of a modified Kozeny-Carmen correlation to characterize hydraulic flow units. *SPE 149047* **2011**; p. 9.
15. Izadi, M., Ghalambor, A. A new approach in permeability and hydraulic-flow-unit determination. *SPE Reservoir Evaluation & Engineering* **2013**, 16, 257–264.
16. Ferreira, F.C.; Booth, R.; Oliveira, R.; Carneiro, G.; Bize-Forest, N.; Wahanik, H. New rock-typing index based on hydraulic and electric tortuosity data for multi-scale dynamic characterization of complex carbonate reservoirs. *In: SPE-175014-MS* **2015**, Houston, Texas, USA.
17. Mirzaei-Paiaman, A.; Ostadhassan, M.; Rezaee, R.; Saboorian-Jooybari, H.; Chen, Z.H. A new approach in petrophysical rock typing. *J. Petrol. Sci. Eng.* **2018**, 166, 445–464.
18. Corbett, P.W.M.; Potter, D.K. Petrotyping: a basemap and atlas for navigating through permeability and porosity data for reservoir comparison and permeability prediction. *SCA2004-30* **2004**; p. 12.
19. Wibowo, A.S.; Permadi, P. A type curve for carbonates rock typing. *Presented at the International Petroleum Technology Conference* **2013**, IPTC-16663-MS.
20. Rezaee, M.R.; Motiei, H.; Kazemzadeh, E. A new method to acquire m exponent and tortuosity factor for microscopically heterogeneous carbonates. *J. Petrol. Sci. Eng.* **2007**, 56, 241–251.
21. Soleymanzadeh, A.; Jamialahmadi, M.; Helalizadeh, A.; Soulgani, B.S. A new technique for electrical rock typing and estimation of cementation factor in carbonate rocks. *J. Petrol. Sci. Eng.* **2018**, 166, 381–388.
22. Mohammadi, M., et al. A novel electrical rock typing approach to improve estimating formation resistivity factor in carbonate rocks. *NIOC Exploration Directorate* **2020**.
23. Mohammadi, M.; Niri, M.E.; Bahroudi, A.; Soleymanzadeh, A.; Kord, S. Development of a new hydraulic electric index for rock typing in carbonate reservoirs. *Scientific Reports* **2024**, 14:18264.
24. Omrani, H.; Hajipour, M.; Jamshidi, S.; Behnood, M. A new method in reservoir rock classification in carbonate and sandstone formations. *J. Geoph. Eng.* **2023**, 20, 883–900.
25. Man, H.Q.; Hien, D.H.; Thong, K.D.; Dung, B.V.; Hoa, N.M.; Hoa, T.K.; Kieu, N.V.; Ngoc, P.Q. Hydraulic flow unit classification and prediction using machine learning techniques: a case study from the Nam Con Son Basin, Offshore Vietnam. *Energies* **2021**, 14, 7714.
26. Mohammadian, E.; Kheirollahi, M.; Liu, B.; Ostadhassan, M.; Sabet, M. A case study of petrophysical rock typing and permeability prediction using machine learning in a heterogeneous carbonate reservoir in Iran. *Scientific Reports* **2022**. 12:4505.
27. Mohammadinia, F.; Ranjbar, A.; Kafi, M.; Keshavarz, R. Application of machine learning algorithms in classification the flow units of the Kazhdumi reservoir in one of the oil fields in southwest of Iran. *J. Petrol. Expl. Prod. Tech.* **2023**, 13, 1419–1434.

 doi:10.20944/preprints202604.1026.v1

28. Astsauri, T; Habiburrahman, M.; Ibrahim, A.F.; Wang, Y. Utilizing machine learning for flow zone indicators prediction and hydraulic flow unit classification. *Scientific Reports* **2024**, 14:4223.
29. Amosu, A.; Bui, D.; Oke, O.; Koray, A.; Kubi, E.A.; Sibaweihi, N.; Ampomah, W. Committee machine learning for electrofacies-guided well placement and oil recovery optimization. *Appl. Sci.* **2025**, 15, 3020.
30. El Sharawy, M.S. Analysis of vertical heterogeneity measures based on routine core data of sandstone reservoirs. *Geosciences* **2025**, 15, 98.
31. Gameel, M.; Darwish, M. Reservoir behavior of the pre- Turonian sandstones in south Gulf of Suez province (Sidki field – case history). *12th EGPC Exploration and Production Conference* **1994**, 2, 449-471.
32. Alsharhan, A.; Salah, M. Lithostratigraphy, sedimentology and hydrocarbon habitat of the Pre-Cenomanian Nubian Sandstone in the Gulf of Suez oil Province, Egypt. *GeoArabia* **1997**, 2, 385-400.
33. Bosworth, W.; McClay, K.R. Structural and stratigraphic evolution of the Gulf of Suez rift, Egypt: a synthesis. In: Zeigler PA, Cavazza W, Robertson AHFR, Crasquin-Soleau S (eds) Peri-Tethys Memoir 6: 'Peritethyan Rift/Wrench Basins and Passive Margins'. Memoires du Museum National d'Historie Naturelle de Paris **2001**, 186; p. 567–606.
34. Montenat, C.; Ott d'Estevou, P.; Jarrige, J.; Richert, J. Rift development in the Gulf of Suez and the northwestern Red Sea: structural aspects and related sedimentary processes. *In: B.H. Purser and D.W.J. Bosence (eds.), Sedimentation and Tectonics of Rift Basins: Red Sea – Gulf of Aden* **1998**; pp. 98-116.
35. El Sharawy, M.S. Seismic and well log data as an aid for evaluating oil and gas reservoirs in the southern part of the Gulf of Suez, Egypt. *Ph.D. Dissertation* **2006**. Mansoura University, Egypt.
36. Omran, M.A.; El Sharawy, M.S. Tectonic evolution of the Southern Gulf of Suez, Egypt: a comparison between depocenter and near peripheral basins. *Arab. J. Geosci.* **2014**, 7, 87–107.
37. Younes, A.I.; McClay, K.R. Role of basement fabric on Miocene rifting in the Gulf of Suez–Red Sea. *EGPC Proceedings of the 14th Petroleum Conference* **1998**, 1, 35–50.
38. Patton, T.L.; Moustafa, A.R.; Nelson, R.A.; Abdine, A.S. Tectonic evolution and structural setting of the Suez rift. *In: Landon SM (ed.), Interior rift basin, AAPG Memoir* **1994**, 59; pp. 9–55.
39. Bosence, D.; Cross, N.; Hardy, S. Architecture and depositional sequences of Tertiary fault-block carbonate platforms, an analysis from outcrop (Miocene, Gulf of Suez) and computer modeling. *Marine and Petroleum Geology* **1998**, 15, 203-221.
40. Schutz, K. Structure and stratigraphy of the Gulf of Suez, Egypt. *In: Landon SM (ed.), Interior rift basin, AAPG Memoir* **1994**, 59; pp. 57-96.
41. Moustafa, A.M. Block faulting in the Gulf of Suez. *EGPC 5th Exploration Seminar* **1976**; p. 36.
42. Egyptian General Petroleum Corporation, EGPC. Gulf of Suez oil fields (A comprehensive overview) **1996**; pp. 736.
43. Chekani, M.; Kharat, R. Reservoir rock typing in a carbonate reservoir cooperation of core and log data: case study. *SPE 123703* **2009**; p. 22.
44. Steinley, D. K-means clustering: A half-century synthesis. *Br. J. Math. Stat. Psychol.* **2006**, 59, 1–34.
45. Bradley, P.S.; Fayyad, U.M. Refining initial points for K-means clustering. *In: Proceedings of the 5th International Conference on Machine Learning* **1998**, 91-99.
46. Tiab, D.; Donaldson, E. Petrophysics: theory and practice of measuring reservoir rock and fluid properties. *Gulf Publishing Company* **2012**, Houston, 950 pp.
47. Nelson, P.H. Permeability-porosity relationship in sedimentary rocks. *Log Analyst* **1994**, 38-62.